ACS Catalysis

pubs.acs.org/acscatalysis

Research Article

Existence and Properties of Isolated Catalytic Sites on the Surface of β-Cristobalite-Supported, Doped Tungsten Oxide Catalysts (WO_x/β-SiO_2, Na-WO_x/β-SiO_2, Mn-WO_x/β-SiO_2) for Oxidative Coupling of Methane (OCM): A Combined Periodic DFT and Experimental Study

Daniyal Kiani, Sagar Sourav, William Taifan, Monica Calatayud, Frederik Tielens, Israel E. Wachs,* and Jonas Baltrusaitis*

Cite This: *ACS Catal.* 2020, 10, 4580−4592

Read Online

ACCESS | Metrics & More | Article Recommendations | Supporting Information

ABSTRACT: The nature of isolated tungsten oxide (WO_x) sites in the dispersed phase on the surface of a β-cristobalite (β-SiO_2) support in undoped and Na- or Mn-doped WO_x/SiO_2 model catalysts used for the oxidative coupling of methane (OCM) has not been explored previously. This work provides a computational model for isolated surface WO_x sites (doped and undoped) supported on β-cristobalite (β-SiO_2) and computationally explores their molecular structure, degree of hydration, and energetics over a wide range of OCM-relevant temperatures from 500 to 1300 K. *Ab initio* thermodynamic analysis showed that the most stable molecular configuration of the surface sites in all cases (WO_x, Na-WO_x, Mn-WO_x) was the digrafted, dioxo pseudotetrahedral WO_4. The thermal stability of the surface WO_4 sites was in the order Na-WO_4 ≫ WO_4 > Mn-WO_4 in the OCM-relevant temperature range of 850−1300 K. A spin analysis of an Mn-WO_4 isolated surface site indicates a paramagnetic high-spin Mn^{2+}−O−W^{6+} electronic state, in line with literature reports. The computed frequencies for isolated surface WO_4 sites agree well with the experimental *in situ* Raman spectra of the corresponding model catalysts, proving their existence. Finally, steady-state OCM studies showed that the C_2 selectivity was highest for Na-WO_4 sites, followed by Mn-WO_4 and WO_4, a trend mimicking the degree of distortion in the molecular geometry of each site. Na-WO_4 exhibited the lowest reactivity toward CH_4 and the highest degree of W═O bond elongation.

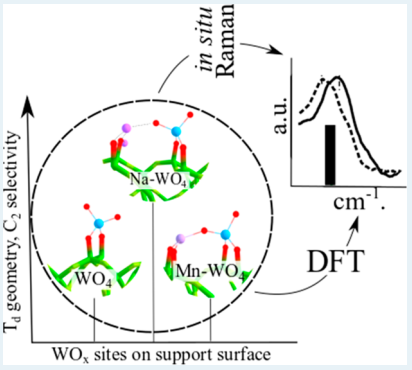

KEYWORDS: *methane, oxidative coupling, tungsten oxide, cristoballite, isolated site, DFT, Raman*

INTRODUCTION

Supported transition-metal oxides are among some of the most important catalytic materials. Specifically, metal and metalloid oxide supported tungsten oxide (WO_x) catalysts have been utilized in numerous catalytic processes of industrial and environmental importance, including hydrocarbon and alcohol upgrading,[1,2,11,3−10] selective catalytic reduction (SCR),[12] olefin metathesis,[13] CO_2 hydrogenation,[14] and production of sulfurous compounds.[15] The ability to synthesize uniform surface WO_x catalytic sites on a support with the desired functionality is of primary importance for obtaining controllable structure−function relationships. In particular, different molecular geometries of the active WO_x surface sites exhibit different catalytic properties.[16−19] The active surface sites present on the support can be isolated, dimeric, oligomeric, or polymeric, which ultimately influences the resulting activity/selectivity and reaction mechanism.[16,20−22] The structure of the active site typically depends on its surface coverage with the maximum amount that can be anchored in a two-dimensional fashion on the support without forming a three-dimensional crystalline phase, defined as the monolayer coverage. The monolayer coverage is routinely used to assess the overall catalyst activity/selectivity of well-defined surface sites.[16,23−25]

One reaction of significance to the natural gas industry is the oxidative coupling of methane (OCM), which converts methane to ethane and ethylene over a heterogeneous catalyst.[26−28] Many supported transition metal oxide catalysts have been tested for OCM with the goal of maximizing ethylene yield and minimizing CH_4 overoxidation to CO and CO_2.[28−33] The SiO_2-supported manganese oxide and sodium tungstate (Mn_xO_y-Na_2WO_4/SiO_2) promoted catalyst is one of the most promising (and one of the most studied) catalysts for OCM due to its thermal stability and ∼30% C_2 yield.[27,28,34,35]

Received: December 27, 2019
Revised: March 6, 2020
Published: March 16, 2020

https://dx.doi.org/10.1021/acscatal.9b05591
ACS Catal. 2020, 10, 4580−4592

In one of the pioneering reports on this catalyst,[36] it was shown that CH_4 conversion did not increase beyond the catalyst loading of 4% Na_2WO_4/SiO_2 by weight. It was concluded, with the aid of XPS surface analysis, that Na_2WO_4 formed as a two-dimensional (2D) dispersed species at up to 4% loading that corresponded to monolayer coverage. At higher loadings, Na_2WO_4 formed 3D crystalline particles, which were proposed to be inactive toward OCM.[36] It was further argued that the active site of this catalyst was the 2D-dispersed tungsten oxide (WO_x) coordinated to Na^+.[37] Subsequent studies aimed to unravel the exact molecular structure and the role of Na-coordinated surface sites via Raman spectroscopy, XRD, and steady-state reactor studies.[37] The Na_2WO_4/SiO_2, WO_3/SiO_2, and Na-WO_3/SiO_2 catalysts, however, were analyzed under ambient conditions, where the catalysts were exposed to air and moisture, both before and after the OCM reaction. It was found that, without Na^+, the supported WO_3/SiO_2 catalyst (prepared from the ammonium para-tungstate precursor in water) was dominated by structures containing an octahedral (O_h) molecular geometry (WO_6) such as those in crystalline WO_3 (Raman bands at 807, 713, and 271 cm^{-1}).[37] The Raman bands for T_d WO_4 from crystalline Na_2WO_4 were found on SiO_2 when Na_2WO_4 in water was employed as the precursor (bands at 927, 811, 788, 416, and 311 cm^{-1}). The addition of Na^+ to the supported WO_3/SiO_2 catalyst led to the disappearance of Raman bands corresponding to O_h WO_6 sites of crystalline WO_3 and the appearance of Raman bands corresponding to the T_d WO_4 sites of crystalline Na_2WO_4, suggesting that the role of Na^+ was that of a structural promoter to retain the T_d coordination of the supported WO_x sites.[37] Fixed-bed reactor studies of model catalysts containing O_h WO_6 vs T_d WO_4 species in OCM were also conducted and showed that the catalysts with T_d Na-WO_4 sites had much higher C_2 selectivity in comparison to those without Na^+ (i.e. O_h WO_6 sites).[37] Other reports have also made similar claims regarding T_d Na-WO_4 sites being active and selective for OCM.[38,39] It is crucial to stress that all such studies reported O_h and T_d units present in the bulk crystalline phases (i.e., WO_3 and Na_2WO_4 nanoparticles, respectively) and not the WO_x surface sites, which are responsible for catalysis and can be drastically different structurally and chemically.[40] In fact, the composition and structure of bulk crystalline materials are known to differ significantly from those of the surface.[41−44] Moreover, the existence of long-speculated crystalline phases is dubious. Recent studies utilizing *operando* XRD-CT (X-ray diffraction computed tomography),[45] *in situ* Raman spectroscopy,[46] and *in situ* XRD[46] have reported that under OCM reaction conditions (675−900 °C, CH_4 + O_2), the 3D-crystalline Na_2WO_4 and Mn_2O_3 phases disappeared as they melted or became reduced.[47] For a more thorough discussion on the molecular structure of active sites, structure−function relationships, properties of the catalysts, the kinetics of catalytic OCM, etc., the reader is referred to a recent in-depth review paper on OCM catalysis.[47]

In contrast, *operando* and *in situ* Raman spectroscopic studies[24,48] of well-defined 2D-dispersed supported WO_x/SiO_2 model catalysts are also available in the literature.[20,21,23,49,50] Such studies have shown that the SiO_2 support surface contains various thermally robust molecular geometries/configurations of surface WO_x sites.[47] For example, the T_d WO_4 ($(O)_2$−W═$(O)_2$) with two double-bonded oxygens (dioxo, digrafted), square-pyramidal WO_5 ($(O)_4$−W═O) with one double-bonded oxygen (mono-oxo, tetragrafted), and oligomeric WO_x chains with W−O−W bridges are just some of the molecular geometries of surface WO_x sites observed on the SiO_2 support.[20,21,23,49,50] Moreover, studies have shown that, under OCM conditions, SiO_2 transforms to the β-cristobalite phase and is not present as the α-cristobalite phase.[51,52] The α-cristobalite phase is only present below 493 K and transforms into the β-cristobalite phase above 493 K, with a 5% volume change.[51−54] Structural differences between the crystalline α- and β-cristobalite supports may strongly affect the distribution and molecular geometry of the active surface site and monolayer coverage on the SiO_2 support catalyst. The α-cristobalite phase has a tetragonal Bravais lattice and belongs to the D_4 point group and $P4_12_12$ space group.[55] On the other hand, the β-cristobalite phase is more ordered, has a cubic Bravais lattice, and belongs to the O_h point group and $Fd3m$ space group.[56] To date, all computational and experimental work has largely ignored the absence of α-cristobalite under OCM conditions since the reported characterization studies were primarily conducted under ambient conditions where the surface is hydrated and SiO_2 support in its α-cristobalite phase. For example, a recent computational report focusing on CH_4 activation on Mn−W oxide clusters supported on a α-cristobalite (111) support found that H abstraction during CH_4 activation was energetically more favorable on Mn═O than on W═O.[57] However, an Mn═O bond has experimentally never been detected for this catalyst, especially at OCM-relevant temperatures. Moreover, the authors assumed that the only role of Na^+ was to restructure the SiO_2 support into the α-cristobalite phase (which does not exist under OCM conditions[51,52]) and that Na^+ had no effect on the WO_x active site in the catalyst. Consequently, Na^+ was not incorporated into the possible active site structures in the computational models.[57] Another study (available only in the Chinese language) used molecular dynamics simulations and *ab initio* DFT to investigate the nature and structure of active sites in Mn_xO_y-Na_2WO_4 on a α-cristobalite (111) support. This study found an unusual WO_4 cluster with three W−O−Si bonds and one W═O bond to be present in α-cristobalite (111).[58] On the basis of the electronic structure and molecular orbital information on this WO_4 site, it was further presumed that the O═W$(-O-Si)_3$ structure is the active site for OCM. However, only T_d WO_4 sites (digrafted. two W−O−Si bonds; dioxo, two W═O bonds) have been experimentally determined and the O═W$(-O-Si)_3$ cluster[58] is not supported by experimental evidence.

Herein, we report computational and experimental results to elucidate the possible molecular and electronic structure of the SiO_2-supported WO_x surface sites on the relevant β-cristobalite phase of the SiO_2 support during OCM. In particular, this study reports on the DFT modeling results of isolated surface sites in uncoordinated, Na-coordinated, and Mn-coordinated tungsten oxide supported on the β-cristobalite phase of SiO_2, WO_x/β-SiO_2, Na-WO_x/β-SiO_2, and Mn-WO_x/β-SiO_2, in conjunction with *ab initio* thermodynamics insights into their thermal stability. Vibrational frequencies were calculated and compared with the experimental *in situ* Raman bands of the well-defined model catalysts. Finally, the steady-state catalytic performance of model bimetal oxide catalysts was tested to understand the effect of the molecular geometry of the surface sites on OCM. The insights regarding structure-function relationships based on model catalysts provided herein shed new light on the possible surface catalytic sites, which are often

https://dx.doi.org/10.1021/acscatal.9b05591
ACS Catal. 2020, 10, 4580−4592

overlooked in the literature on Mn_xO_y-Na_2WO_4/SiO_2 catalysts for OCM.

EXPERIMENTAL AND COMPUTATIONAL METHODS

DFT Calculations. The periodic calculations have been performed with the Vienna Ab Initio Simulation Package (VASP)[59−62] using the Perdew and Wang (PW91) generalized gradient approximation exchange-correlation functional.[63] The valence electrons are treated explicitly, and their interactions with the ionic cores are described by the Projector Augmented-Wave (PAW) method,[15,59,64] which allows using a low-energy cutoff equal to 400 eV for the plane-wave basis. A sampling of the Brillouin zone with 2 × 2 × 1 mesh was applied for all models in this work. The positions of the two topmost layer atoms, as well as the active (un)coordinated WO_x site, in the supercell were relaxed until the total energy differences decrease below 10^{-6} eV (forces acting on atoms fall below 0.005 eV/Å).

Vibrational spectra have been calculated for the selected surface species within the harmonic approximation. Only the tungsten center and its first and second neighbors (O−Si and OH groups) were considered in the Hessian matrix. This matrix was computed by the finite difference method followed by a diagonalization procedure. The eigenvalues of the resulting matrix led to frequency values. The assignment of the vibrational modes was done by inspection of the corresponding eigenvectors. The details of the model of the hydroxylated β-cristobalite slab can be found elsewhere.[64] Briefly, the β-cristobalite surface was modeled by a slab, constructed by cutting the bulk parallel to the (001) and (110) crystallographic planes. The surface unit cell dimensions (Å) are a = 15.21, b = 10.14, and c = 28.00 (including 20 Å of vacuum) for the (001) plane.

Ab initio constructed phase diagrams (surface energy (γ) vs temperature (T)) were generated according to details provided elsewhere.[64] Briefly, it was assumed that there was no variation in the chemical potential of the surface upon the adsorption of sites and that the gas phase is a perfect gas. In the proposed scheme, the free energy of water (including the zero-point energy, ZPE, correction) in the gas phase was calculated by eq 1

$$G^{\text{Gaussian}}_{\text{Temp.Corr.}}(H_2O) = E(H_2O) + ((\Delta H_G - T\Delta S_G(T)) + RT\ln(P/P^0)) \quad (1)$$

where $E(H_2O)$ is the electronic energy of water calculated at 0 K, ΔH_G and $\Delta S_G(T)$ are the enthalpy and entropy corrections of gaseous water, respectively, calculated with Gaussian03[65] in the temperature range 500−1300 K. P is the partial pressure of water vapor[66] and P^0 is the standard pressure (1 bar).

The area normalized E_{ads} of the condensed phase was added to the area normalized $G^{\text{Gaussian}}_{\text{Temp.Corr.}}(H_2O)$ to calculate surface energy in J mol^{-1} m^{-2} of a configuration, as shown in eq 2. Note that only the $G^{\text{Gaussian}}_{\text{Temp.Corr.}}(H_2O)$ value depends on T and P; therefore, energies of the condensed phase will not depend on the temperature.[64] The final value is the sum of condensed and vapor phases, with the vapor phase values corrected for temperature. The surface energy (γ) calculations are summarized in eqs 2−4.

$$\gamma\ (\text{J molecule}^{-1}\ \text{m}^{-2}) = \frac{\Delta E_{ads}}{\text{area of slab}\ (\text{m}^2)} + n(G^{\text{Gaussian}}_{\text{Temp.Corr.}}(H_2O))\ (\text{J molecule}^{-1}) \quad (2)$$

$$\Delta E_{ads}\ (\text{J molecule}^{-1}) = E_0^{\text{DFT}}(\text{products}) - E_0^{\text{DFT}}(\text{reactants}) \quad (3)$$

$$n\ (\text{m}^{-2}) = \frac{\#\ \text{of}\ H_2O\ \text{exchanging with gas phase}}{\text{area of slab}\ (\text{m}^2)} \quad (4)$$

Well-Defined Model Catalyst Site Synthesis and Molecular Structural Characterization with *In Situ* Raman Spectroscopy. The supported catalysts were prepared by incipient-wetness impregnation of aqueous ammonium metatungstate ($(NH_4)_{10}W_{12}O_{41}\cdot xH_2O$ (Alfa Aesar, Product #44792)), manganese nitrate ($Mn(NO_3)_2$ (Alfa Aesar, Product #10806-09), and sodium hydroxide (NaOH (EMD MilliPore, Product #1064621000)) onto a SiO_2 support (Cabosil, EH-5). After impregnation, the samples were initially dried at room temperature overnight and then at 393 K in flowing air (150 mL/min) in a calcination oven for 2 h and finally calcined in flowing air (150 mL/min) for 4 h at 500 °C. The silica-supported tungsten oxide catalysts were prepared with 5% WO_x, 0.4% Na/8% WO_x, and 1% Mn/5% WO_x (metal basis). Specifically, the 5% WO_x/SiO_2 catalyst was chosen as it corresponds to the highest achievable concentration of surface WO_x (x = 4, 5) sites in the dispersed phase before the crystalline WO_3 phase can form. The 8% WO_x/0.4% Na/SiO_2 catalyst was prepared according to a recently published report on Na-enhanced dispersion,[16] such that the molar ratio Na/W was ∼0.4, which ensures that crystalline Na_2WO_4 does not form and the Na-WO_4 sites are dispersed. Finally, the 1% Mn/5% WO_x/SiO_2 catalyst was prepared to mimic the undoped 5% WO_x/SiO_2 catalyst. Regardless of the Mn loading, an $MnWO_4$ crystalline phase coexisted with the dispersed Mn-WO_4 sites on the SiO_2 surface.

The *in situ* Raman spectra of the catalysts were obtained with a Horiba LabRam HR instrument equipped with a 442 nm laser and a liquid N_2 cooled CCD detector (Horiba CCD-3000 V). The spectral resolution was approximately 1 cm^{-1}, and the wavenumber calibration was checked using the silica standard line at 520.7 cm^{-1}. The laser was focused on the catalyst samples with a confocal microscope using a 50× objective (Olympus BX-30-LWD). Typically, the spectra were collected with 15 s/scan with a total of six scans. Approximately 5−25 mg of each catalyst in powder form was loaded into an environmental cell (Harrick, HVC-DR2) that was sealed with O-ring seals, which was kept cool by flowing water. The *in situ* Raman spectra of the dehydrated catalysts were collected at 673 K, after 673 K dehydration in 10% O_2/Ar for 60 min.

It is important to note that only the Na-containing sample undergoes a transformation of amorphous SiO_2 to crystalline cristobalite, and the absence of Na in the supported WO_x/SiO_2 and Mn-WO_x/SiO_2 catalysts retains SiO_2 in the amorphous phase. Amorphous SiO_2, in the absence of Na, does not transition to the crystalline cristobalite phase until temperatures above 1743 K, but the transformation temperature is decreased to ∼1273 K with Na, which is within the OCM reaction temperature.[51,52]

https://dx.doi.org/10.1021/acscatal.9b05591
ACS Catal. 2020, 10, 4580−4592

OCM Catalytic Testing. The OCM performance of the model catalysts was tested under steady-state reaction conditions in an Altamira Instruments temperature-programmable system (AMI-200) equipped with an online quadrupole MS (Dycor Dymaxion, DME100MS). Typically, ~30 mg of the catalyst was loaded into a U-shaped quartz tube (4 mm i.d.) and held in place by quartz wool plugs. The catalyst was initially calcined at 673 K in a 10% O_2/90% Ar mixture (Airgas certified, 30 mL/min) for 60 min to remove adsorbed moisture and any combustible impurities that might be present. Then, the temperature was ramped up to 1173 K at 20 K/min. Upon reaching 1173 K under 10% O_2/90% Ar, the system was flushed with Ar before the gas mixture was switched to 25 mL/min of CH_4 and 40 mL/min of air (Air Products, ultra zero grade), and these conditions were maintained for 2 h. Next, the temperature was decreased to 1103 K, and another gas matrix (5 mL/min of CH_4, 15 mL/min of 10% O_2/90% Ar, 80 mL/min of Ar; WSHV ~200000 g^{-1} h^{-1}) was introduced and the conditions were maintained for 2 h, during which data were collected. All data were collected using an online mass spectrometer. The OCM reaction was conducted using low oxygen concentration with $CH_4/O_2 \approx 3.3$ to prevent oxidation of the MS filament and to minimize heat and mass transfer effects. The reactivity was calculated as

$$\text{reactivity } (\mu\text{mol g}^{-1}\text{ h}^{-1}) = \frac{\chi \times [CH_4] \times Q \text{ (L h}^{-1})}{\frac{24L}{\text{mol}} \times \text{catalyst (g)} \times \text{loading}_{\text{tungsten}}}$$

RESULTS AND DISCUSSION

The Hydroxylated β-Cristobalite Model. A detailed description of the hydroxylated β-cristobalite (001) surface computational model used herein can be found elsewhere.[67] Briefly, the Si−O and O−H bond lengths were 1.62 and 0.97 Å, respectively. The model used is shown in Figure 1 and can be represented by the formula $(SiO_2)_x{\cdot}yH_2O$. Specifically, the supercell of the model has the formula $Si_{24}O_{57}H_{18}$, which can be written as $(SiO_2)_{24}(H_2O)_9$. The slab had a surface area of 1.542 nm^2.

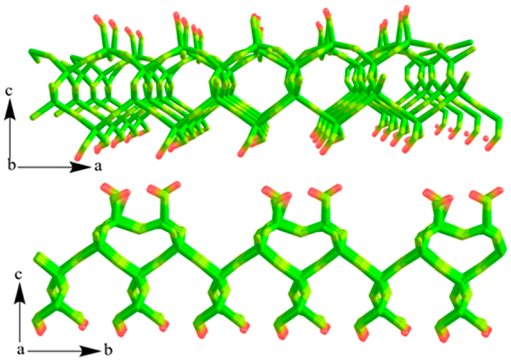

Figure 1. Hydroxylated β-cristobalite (001) slab used in this study. Monomeric species (such as WO_x) were anchored on the (001) surface plane. Color code: Si, green; O, yellow; H, red.

WO_x/β-SiO_2: Molecular Structure and Thermal Stability of the Isolated Surface Sites. Various configurations of tungsten oxide molecular structures grafted onto the β-SiO_2 (001) surface are possible, as shown in Figure S1. The β-SiO_2-supported WO_x surface species can be obtained according to the reaction given in eq 5

$$H_2WO_4 + (SiO_2)_{24}{\cdot}9H_2O \rightarrow Si_{24}O_{61-n}H_{20-2n}W + nH_2O \quad (5)$$

where n is the number of water molecules exchanging with the gas phase (−1 to +3). For example, configuration A represents a surface site with one W−O−Si bond, five W−OH bonds, no W═O bond, and $n = -1$; therefore, eq 5 for configuration A can be written as

$$H_2WO_4 + (SiO_2)_{24}{\cdot}9H_2O \rightarrow Si_{24}O_{62}H_{22}W - H_2O \quad (6)$$

All bond parameters, including their number and type as well as the number of H_2O molecules involved in the overall formation reaction for each configuration, and the resulting equations are summarized in Table S1. Since the experimentally determined maximum loading of 2D-dispersed surface WO_x sites on amorphous SiO_2 is 0.5 W atoms/nm^2,[20,21,68] one WO_x unit was anchored per entire slab, resulting in ~0.6 W_{atoms}/nm^2 coverage.[21] The varieties of the adsorption configurations that were explored are due to the number of adjacent silanol groups on the β-SiO_2 (001) surface involved in grafting, the number of oxo bonds (W═O), and the number of W−OH bonds. For example, configuration A shows monografted tungsten oxide sites without oxo bonds. Likewise, the configuration I shows tetragrafted, mono-oxo tungsten oxide sites.

In order to understand the thermal stability of various β-SiO_2 (001) grafted molecular geometries possible for the WO_x species, *ab initio* thermodynamics were used to calculate the corresponding surface energy for each binding configuration in J $molecule^{-1}$ m^{-2}, which is the thermally corrected Gibbs energy per molecule, normalized by the surface area of the β-SiO_2 (001) slab. Assuming that the surface is in thermodynamic equilibrium with the gas phase, the chemical potential of all species is related to temperature and pressure.[64] The results of the computed surface energies for the three most stable β-SiO_2 (001) grafted WO_x geometries are shown in Figure 2. At temperatures between 500 and 675 K, configuration E ($WO_3(OH)_2$: digrafted, mono-oxo, two W−O−H bonds) was the most stable and dominant site. At higher temperatures (675−1300 K), however, the most stable and dominant configurations were F (WO_4: digrafted, dioxo) and I (WO_5: tetragrafted, mono-oxo). This is in agreement with the experimental *in situ* Raman spectroscopy studies of SiO_2-supported WO_x catalysts, where the existence of I (mono-oxo) and F (dioxo) WO_x configurations have been shown.[17,21,48,69] The mono-oxo species, with a shorter W═O bond length, exhibits a Raman band at ~1015 cm^{-1}, while the dioxo species with its slightly elongated W═O bonds exhibits a Raman band at ~985 cm^{-1}.[17,21,48,69] It should also be noted that it is known from *in situ* X-ray absorption near edge spectroscopy (XANES) measurements that the configuration F is the dominant surface tetragrafted tungsten oxide site on the amorphous SiO_2 surface[24] under dehydrated conditions.

The characteristic bond lengths of the thermally stable configurations (E, F, and I) are summarized in Figure 2. The bridging (W−O)−Si bond lengths in E, F, and I were 1.93, 1.89, and 1.92 Å, respectively. The terminal (W═O) bond lengths in E, F, and I were 1.72, 1.73, and 1.70 Å, respectively, which fall within the reported W═O length range.[63] Finally, only configuration E possessed the W−OH functionality, with a bond length of 1.92 Å. Thus, all of the stable structures

https://dx.doi.org/10.1021/acscatal.9b05591
ACS Catal. 2020, 10, 4580−4592

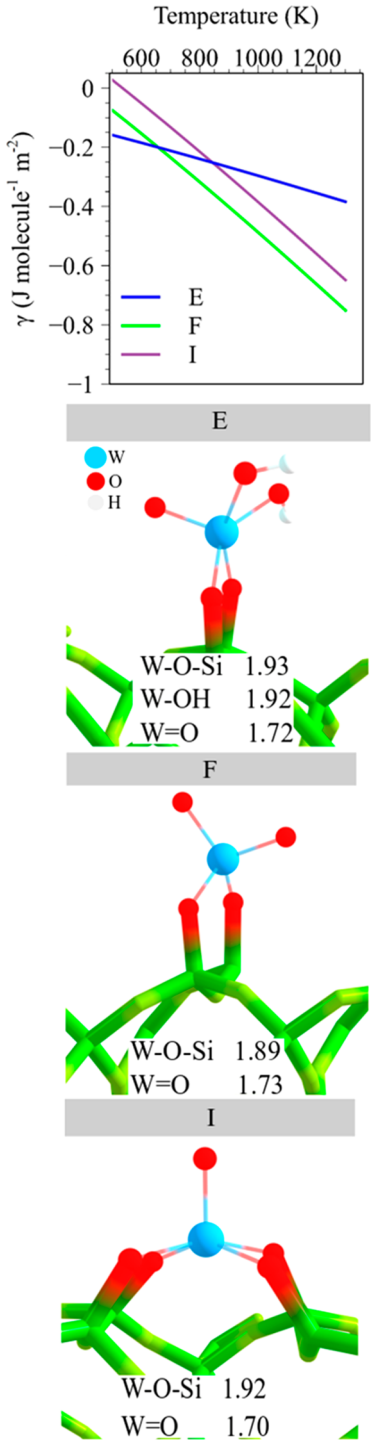

Figure 2. *Ab initio* thermodynamic phase diagram (surface energy vs T) of the most stable surface WO_x molecular geometries. Thermally stable, optimized molecular structures with characteristic bond lengths in Å are also shown.

exhibited similar bond lengths for the same functionality. At temperatures above ~850 K, the degree of hydration decreased and W−OH bonds were not present in configurations F and I. The temperature dependence of surface molecular geometry (dioxo vs hydrated sites) was recently evidenced in an experimental report and matches the trend observed in this study that at higher temperatures the surface dioxo structure becomes dominant.[70]

Na-WO_x/β-SiO_2: Molecular Structure and Thermal Stability of the Isolated Surface Sites. Various configurations of Na-WO_x molecular structures grafted on the β-SiO_2 (001) surface are possible and are shown in Figure S2. The models of Na-WO_x/β-SiO_2 were constructed following eq 7

$$Na_2WO_4 + (SiO_2)_{24}\cdot 9H_2O \rightarrow Si_{24}O_{61-n}H_{18-2n}WNa_2 + nH_2O \quad (7)$$

where n is the number of water molecules exchanged with the gas phase (2 to −1) for isolated Na_2WO_4 grafts. For example, configuration E-1 represents a surface site with two W−O−Si bonds, two W═O bonds, one W−OH bond, two Na−O−Si bonds and n = +1; therefore, eq 6 can be written as Na_2WO_4 + $(SiO_2)_{24}\cdot 9H_2O \rightarrow Si_{24}O_{60}H_{16}WNa_2 + H_2O$. Bond structural parameters and resulting reaction equations are summarized in Table S2 for all Na-WO_x configurations. The reason for the configurational variety within the single W−O−Si bonding configuration arises from the possible modes of Na coordination: two Na atoms coordinated to W−O (W−O−Na) with one Na atom coordinated to Si−O (Si−O−Na) while the other Na atom is coordinated to W (W−O−Na) and both Na atoms are coordinated to Si−O (Si−O−Na).

The *ab initio* thermodynamics surface energy as a function of temperature was calculated to probe the thermal stability of the possible molecular configurations, and the results for the three most stable structures are shown in Figure 3. In the temperature range 500−1300 K, the most stable configuration was found to be F (digrafted, dioxo), followed by G-1 (digrafted, mono-oxo, one W−OH) and E-3 (digrafted, mono-oxo). Note that in Figure 3 it is hard to differentiate between G-1 and E-3, as the surface energy values are similar, but G-1 is lower in surface energy at all temperatures. The surface energies of G-1 and E-3 configurations were close to each other at all temperatures, though G-1 was slightly more thermally stable. The molecular structures and characteristic bond lengths of the stable configurations (G-1, E-3, and F) are summarized in Figure 3. The (W−O)−Si bond lengths in G-1, E-3, and F configurations were 2.01, 2.13, and 1.88 Å, respectively. The W═O bond lengths in E-3 and F were 1.79, 1.74 Å, respectively. Only G-1 had a W−OH functional group with a bond length of 1.93 Å. The (W−O)···Na bond lengths in G-1, E-3, and F were 1.77, 1.78, and 1.75 Å, respectively. Finally, the (Na−O)···Si bond lengths were 2.20, 2.42, and 2.30 Å for G-1, E-3, and F, respectively. From the characteristic bond length comparison, it is interesting to note that configuration F exhibited the shortest W═O bond, the shortest W−O−Si bond, and the shortest (W−O)···Na interatomic distance. It is known that the strong interaction of a base such as K^+ or Na^+ with the surface WO_x site would lead to elongation of the W═O bonds, as seen by the red shift of the W═O Raman band from 985 to 963 cm^{-1} with increasing K^+ content, reported in recent studies on a K-doped WO_x/Al_2O_3 catalyst.[15,18] Configuration F exhibited the weakest interaction of Na^+ with the surface WO_x site, as it had the shortest W−O and W═O bonds. Interestingly, the bridging (Na−O)−Si bond length for configuration F was intermediate to those of G-1 and E-3, which hints at an intermediate level of Na^+ interaction with the surface Si−O. Finally, in the presence of Na^+, only one out of three thermally stable configurations exhibited W−OH bonds (i.e. G-1) since Na^+ functions as a strong Lewis base[18] to neutralize the

https://dx.doi.org/10.1021/acscatal.9b05591
ACS Catal. 2020, 10, 4580−4592

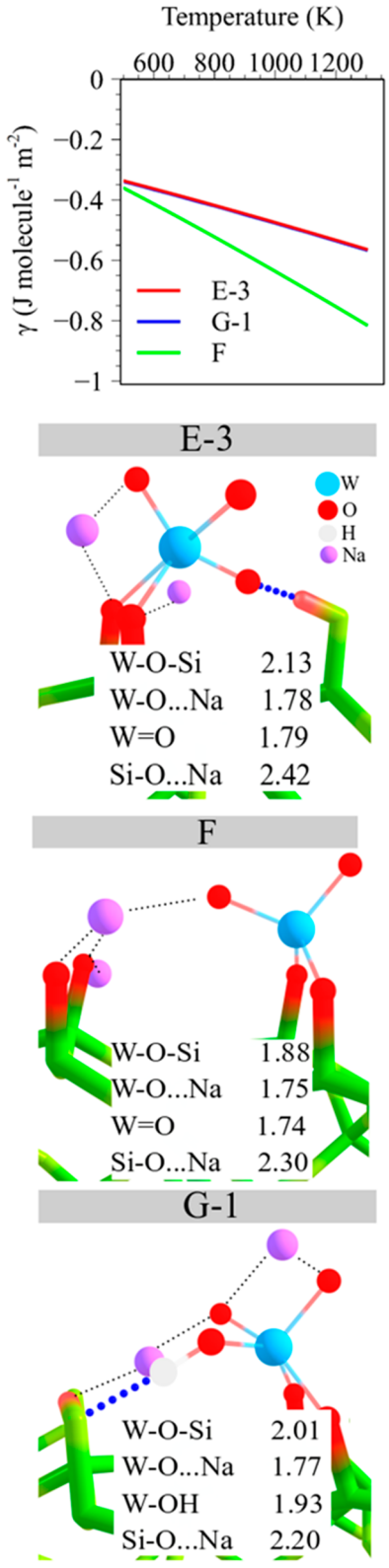

Figure 3. *Ab initio* thermodynamics phase diagram (surface energy vs T), showing thermal stability of Na-WO_x grafted molecular geometries. Thermally stable, optimized molecular structures with characteristic bond lengths in Å are also shown. Note: it is challenging to differentiate between G-1 and E-3, as the surface energy values are similar, but G-1 is slightly lower in surface energy at all temperatures.

hydrogen in the Si−OH groups to form the bridging $(Si-O)^{-}Na^{+}$ bond.

Mn-WO_x/β-SiO_2: Molecular Structure and Thermal Stability of the Isolated Surface Sites. Multiple configurations of Mn-WO_x molecular structures are possible, as shown in Figure S3. The structural models were constructed following eq 8

$$MnWO_4 + (SiO_2)_{24}\cdot(H_2O)_9 \rightarrow Si_{24}O_{(61-n)}H_{(18-2n)}WMn + n\cdot H_2O \quad (8)$$

where n is the number of water molecules exchanged with the gas phase (2 to −1) to graft the surface sites. For example, configuration *C-1* represents surface site with one W−O−Si bond, two W═O bonds, one W−OH bond, two Mn−O−Si bonds, and n = +1, so eq 7 becomes $MnWO_4 + (SiO_2)_{24}\cdot(H_2O)_9 \rightarrow Si_{24}O_{60}H_{16}WMn+H_2O$. Parameters and resulting equations for all configurations are summarized in Table S3.

The *ab initio* thermodynamics-based surface energy as a function of temperature was calculated for each configuration, and the results of the three most stable configurations are presented in Figure 4. At temperatures between 500 and 1300 K, the most thermally stable configuration was F (Mn-WO_4: digrafted, dioxo). The second most stable configuration in the temperature range 500−550 K was the digrafted DX-3, and above 550 K configuration G-1 (digrafted, mono-oxo) became the second most stable. The characteristic bond lengths of the most stable configurations (D-3, F, G-1) are summarized in Figure 4. The (W−O)−Si bond lengths in configurations D-3, F, and G-1 were 2.03, 1.87, and 1.94 Å, respectively. The W═O bond length in F was 1.72 Å, while in D-3 and G-1 the W−OH functional group was present with W−O bond lengths of 1.96 and 1.91 Å, respectively. Moreover, the (W−O)···Mn bond lengths were 2.01, 1.79, 1.81 Å, for D-3, F, and G-1, respectively. Finally, the Mn−O···Si bond lengths were 2.27, 1.90, and 1.84 Å, respectively. The characteristic bond length comparison among the stable configurations shows that the most thermally stable configuration F, which represents Mn-WO_4, had the shortest (W−O)···Mn bond (i.e., Mn^{2+} interacted weakly with the WO_4 unit in this case). Moreover, configuration F also exhibited the shortest (W−O)−Si bonds, indicating strong grafting of the species to the silica support. The Mn−O−Si bond length in configuration F was intermediate to that in configurations D-3 and G-1, suggesting an intermediate degree of the Mn^{2+} interaction with the surface Si−OH groups. It should be noted that, in the presence of Mn, two out of the three thermally stable configurations, namely D-3 and G-1, exhibited W−OH bond(s), indicating that, unlike Na^{+}, Mn^{2+} did not function as a strong Lewis base.

Effect of Dopant on the Thermal Stability and the T_d Geometry of WO_4 Surface Sites. Configuration F representing the T_d WO_4 (digrafted, dioxo) molecular geometry was the most thermally stable in each case: i.e., WO_4, Na-WO_4, and Mn-WO_4. It is worthwhile to compare the structures and properties of such WO_4 sites in each case, as different dopants interact with and alter the WO_4 geometry to varying extents, which can affect the activity of such isolated surface sites toward OCM.[37,71] To probe the *relative* thermal stability of configuration F among the different catalysts studied herein, the differences in surface energy of uncoordinated WO_4 and M-coordinated WO_4 (M = Na, Mn) were computed as a function of temperature. Positive difference values imply greater thermal stability, and negative difference values imply lower thermal stability in comparison to the uncoordinated WO_4 sites. At all temperatures between 500 and

https://dx.doi.org/10.1021/acscatal.9b05591
ACS Catal. 2020, 10, 4580−4592

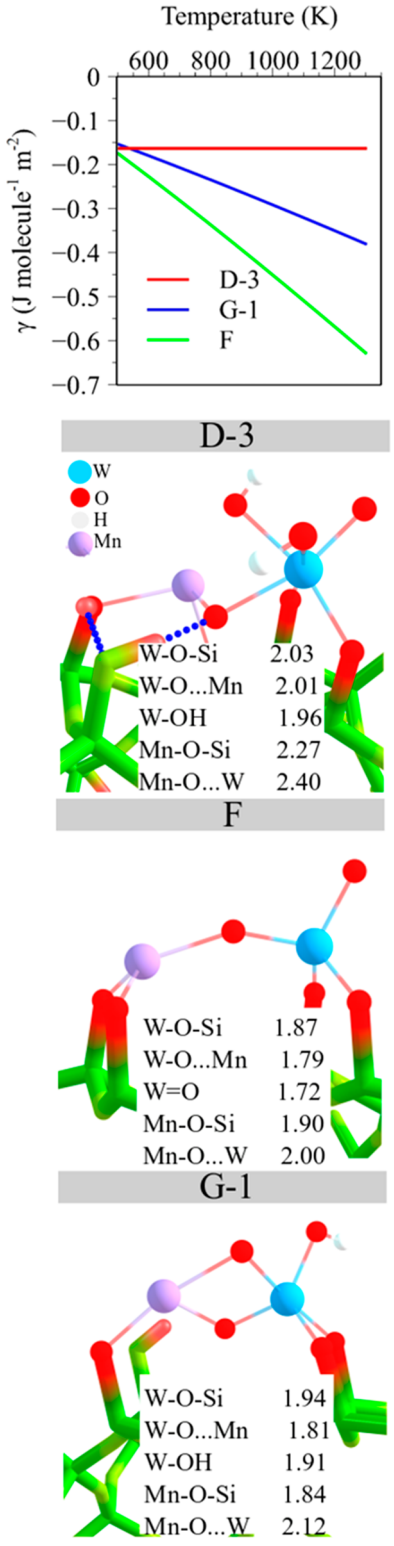

Figure 4. *Ab initio* thermodynamics phase diagram (surface energy vs T), showing the stability of stable Mn-WO_x configurations. Thermally stable, optimized molecular structures with characteristic bond lengths in Å are also shown.

1300 K, the Na-WO_4 site is thermally more stable than the uncoordinated WO_4 site, as depicted in Figure 5a. The Mn-WO_4 site was thermally more stable than uncoordinated WO_4 between 500 and 850 K, but it becomes less stable above 850 K. Finally, the Na-WO_4 site is thermally more stable than the Mn-WO_4 and WO_4 sites at all temperatures (500−1300 K).

The surface WO_4 geometry has been suggested to be a key parameter toward making the surface WO_x site-selective toward C_2 products during OCM,[37,38] and thus it is worthwhile to compare how the surface WO_4 units differed geometrically for each case. The dotted line in Figure 5b represents the ideal 109.47° angle expected for a perfect T_d structure. However, crystalline Na_2WO_4 possesses irregular, distorted WO_4 units, as discussed at length in a literature report.[72] The average tetrahedral angles for surface WO_4, Na-WO_4 ,and Mn-WO_4 sites on the β-SiO_2 (001) support were 108.6, 110.4, and 108.4°, respectively. The variance in angles in each case is shown as an error bar in Figure 5b. In all three cases, the average angle was close to 109.5°; therefore, the WO_4 site in each case can be regarded as pseudotetrahedral since it is slightly distorted from the ideal T_d geometry. The variance and the distortion are large in the case of surface WO_4 and Mn-WO_4 (variance ±4.35°) and smaller for Na-WO_4 (±1.35°). The weak interaction between Mn^{2+} and W^{6+} makes the presence of the bridging Mn−O−W bond less probable. In the presence of both Na^+ and Mn^{2+} (not modeled herein), extrapolation suggests that the surface WO_4 site will most likely be Na coordinated and not Mn coordinated.

Electronic Structure of the Most Thermodynamically Stable, Isolated Mn-WO_4 Surface Site F. Recent *in situ* Raman measurements have shown that Mn^{3+} reduction is much easier than W^{6+} reduction and Mn-related paramagnetic species might be present during OCM.[46,73] During electronic structure calculations, the spin was allowed to relax and converged to five unpaired electrons: 4.53 e^- on Mn, 0.14 e^- on W, and the rest on the neighboring O sites, according to a Bader spin density analysis.[74−76] This indicates the Mn^{2+}-W^{6+} electronic state, where Mn carries most of the unpaired electrons (shown in the inset of Figure 6a). However, small contamination of the Mn^{3+}-W^{5+} electronic state cannot be ruled out. Figure 6a shows the total and the atom-projected densities of states (DOSs). The atom-projected DOS plots show that the valence band minimum is composed of localized Mn 3d states, while the conduction band minimum of the empty W 5d states and the calculated band gap is ∼4.5 eV. In the literature, a DOS analysis of crystalline phase $MnWO_4$ (octahedral MnO_6 and WO_6 units, wolframite structure) showed that the valence band minimum was populated by the highly localized Mn 3d states, while the conduction band minimum by empty W 5d; with a band gap of ∼2.7−3.0 eV.[77] Given the localized transition-metal d states at both the valence and conduction bands, the formation of holes (Mn^{3+} at a Mn^{2+} site) and electron polarons (W^{5+} at the W^{6+} site) is expected in these systems[77]—more so in the crystalline phase $MnWO_4$. The key difference is the larger band gap of ∼4.5 eV of the dispersed phase Mn-WO_4 site owing to its pseudotetrahedral, isolated nature in contrast to the highly coordinated, octahedral WO_6 sites in crystalline $MnWO_4$. It is expected that these dispersed phase isolated sites will differ in catalytic properties from the crystalline $MnWO_4$ owing to their unique molecular and electronic structures. Charge density difference plots of WO_4 and Mn-WO_4 structures are shown in Figure 6b,c, respectively. It can be seen that there is a significant charge transfer to the terminal W═O moiety, shown in yellow in the WO_4 structure, as opposed to that in Mn-WO_4. The charge transferred away from the terminal W═

https://dx.doi.org/10.1021/acscatal.9b05591
ACS Catal. 2020, 10, 4580−4592

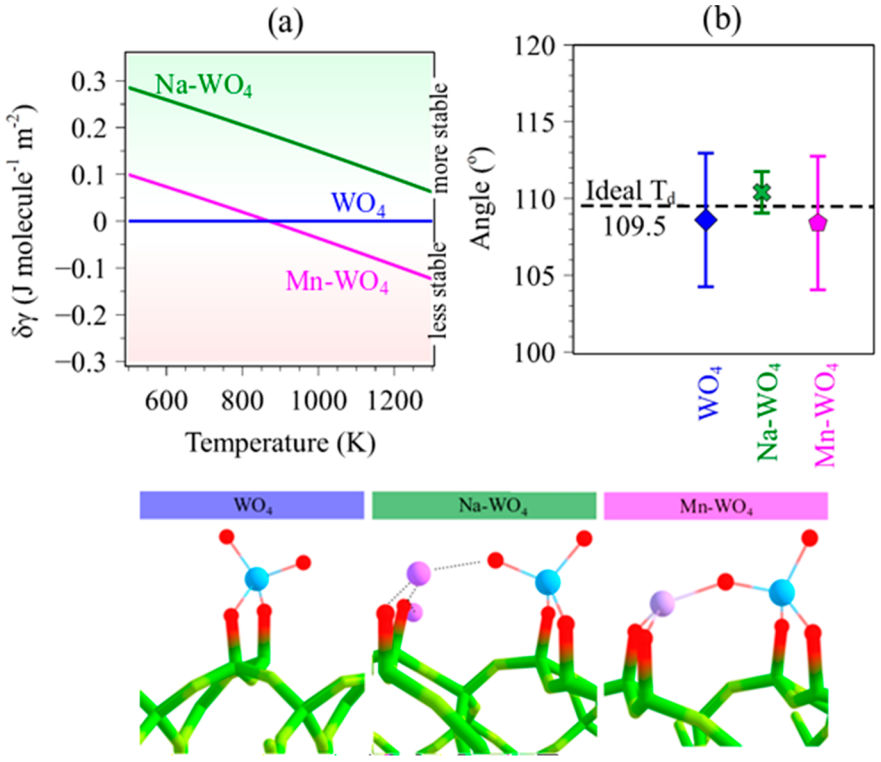

Figure 5. (a) Surface energy difference ($\delta\gamma = \gamma(WO_4) - \gamma(M\text{-}WO_4)$) as a function of temperature between uncoordinated WO_4 and M-WO_4 (M = Na (green), Mn (pink)). The blue dotted line at the origin is used as a reference and represents the surface energy difference between two uncoordinated WO_4 sites ($\gamma(WO_4) - \gamma(WO_4)$). Positive values of $\delta\gamma$ signify greater thermal stability. (b) Comparison of T_d angles in configuration F for WO_4, Na-WO_4, and Mn-WO_4, with reference to crystalline Na_2WO_4.

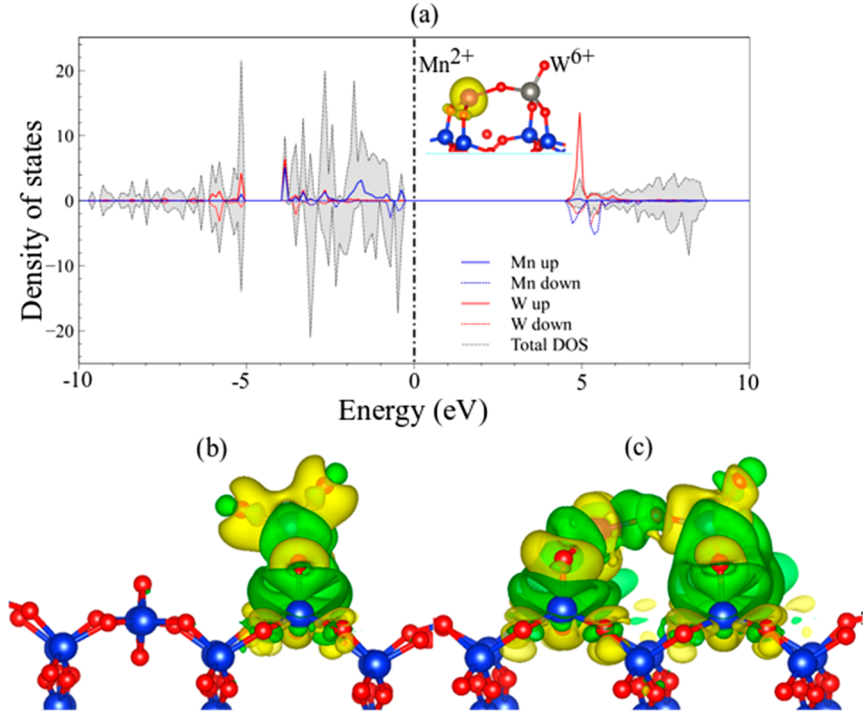

Figure 6. (a) Total (black) and atom-projected densities of states (DOS) (blue and red, respectively) around the Fermi level (0 eV, dashed line) for the thermally stable F site model in the silica-supported Mn-WO_4 catalyst. The positive and negative values of DOS represent up and down spins, respectively. Inset: spin density isosurface (yellow), showing that the unpaired electrons are mainly localized on the Mn site. (b, c) cCharge density difference plots of WO_4 and Mn-WO_4 structures, respectively. The isodensity value was set to 0.001. Positive values (electron density gained) are shown in yellow, while negative values (electron density lost) are shown in green.

https://dx.doi.org/10.1021/acscatal.9b05591
ACS Catal. 2020, 10, 4580−4592

O bond in Mn-WO_4 appears to be distributed predominantly on the Mn−O−W junction and results in its elongation.

Calculated and Experimental Frequency Comparison for Surface WO_4 Sites on β-SiO_2 (001). The computed frequencies of the tungsten−oxo (W═O) bond for SiO_2-supported WO_x, Na-WO_x, and Mn-WO_x catalysts were compared to the corresponding experimental Raman frequencies, as shown in Figure 7. The experimental data used herein

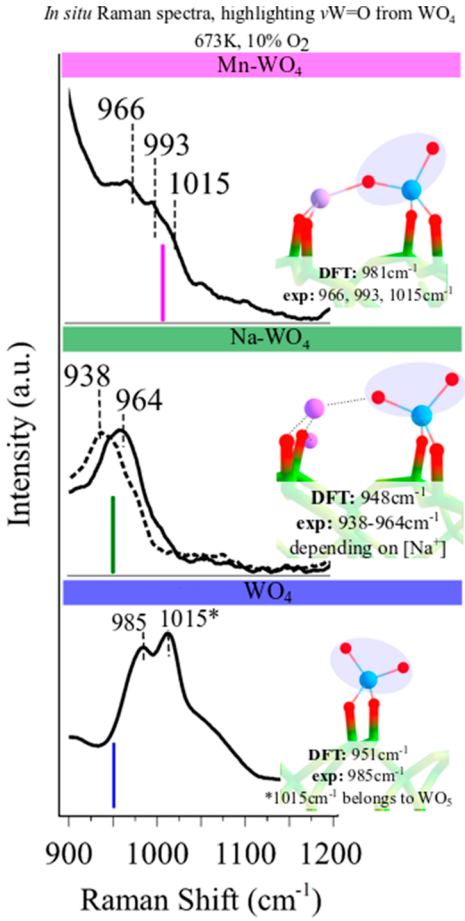

Figure 7. Comparison of experimental Raman spectra (dehydrated samples, 673 K, 10% O_2 in Ar), with computed frequencies (arbitrary intensity, no scaling). Colored bars (blue, 951 cm^{-1}; green: 945 cm^{-1}; pink, 981 cm^{-1}) are the computed frequencies for the W═O stretching in WO_4 units in each case. Full spectra are shown in Figure S4.

were acquired at 673 K under dehydrated conditions with 10% O_2/90% Ar. For supported WO_x/SiO_2, Raman bands at 1015 and 985 cm^{-1}, corresponding to WO_5 and WO_4 species, respectively, were observed. The corresponding computed frequency of the W═O bonds in the WO_4 (F) unit was 950 cm^{-1}, shown with a blue bar in Figure 7. In the case of Na-WO_x/SiO_2, the experimental Raman band for Na-WO_4 was observed at ∼950 cm^{-1}, but higher Na^+ concentrations further shifted the band toward even lower wavenumbers (i.e., toward the 927 cm^{-1} Raman band of the crystalline Na_2WO_4).[78] The computed Na-WO_4 (F) stretching frequency was 945 cm^{-1} and matches well with the experimental Raman frequency. Finally, Mn-WO_x/SiO_2 exhibited a weak and broad experimental Raman band at ∼966 cm^{-1}, while the computed Mn-WO_4 vibrational frequency was 981 cm^{-1}. The DFT calculated fundamental vibrational frequency values for the surface WO_4 sites are in good agreement with the high-temperature *in situ* Raman frequencies. Moreover, the calculated frequencies and the *in situ* Raman spectra corroborate that uncoordinated versus Na-coordinated versus Mn-coordinated isolated WO_4 surface sites exhibit observably different molecular geometries. The W═O bond elongates as Na or Mn coordination occurs, as evidenced by the red shift of the W═O experimental Raman band. It is important to note that, in the case of the surface Na-WO_x catalyst, the only band present is 964 cm^{-1}. However, in the case of the surface Mn-WO_x catalyst, a broad, ill-defined band with shoulders at 966, 993, and 1015 cm^{-1} is observed, which implies weaker coordination and the coexistence of uncoordinated surface WO_x and Mn-coordinated WO_x sites. In the case of the Mn-WO_x catalyst, a sharp and intense band at 885 cm^{-1} corresponding to crystalline $MnWO_4$ was also observed (not shown in the figure to highlight the surface Mn-WO_x species). The *in situ* Raman spectra also corroborate the *ab initio* thermodynamics calculations and show that surface WO_4, Na-WO_4, Mn-WO_4 sites do exist and are stable at 673 K.

Steady-State OCM Reactivity Tests. The steady-state catalytic OCM results of the model SiO_2-supported WO_x, Na-WO_x, and Mn-WO_x catalysts are summarized in Figure 8 and Table S4. The C_2 selectivity of the Na-WO_x catalyst was the highest (80.4%), followed by Mn-WO_x (67.5%) and WO_x (66.5%). Reactivities (based on CH_4 conversion) for WO_x, Na-WO_x, and Mn-WO_x catalysts were 0.185, 0.110, and 0.168 $\mu mol_{CH4}\ h^{-1}\ g_W^{-1}$, respectively. The C_2 yields for the silica-

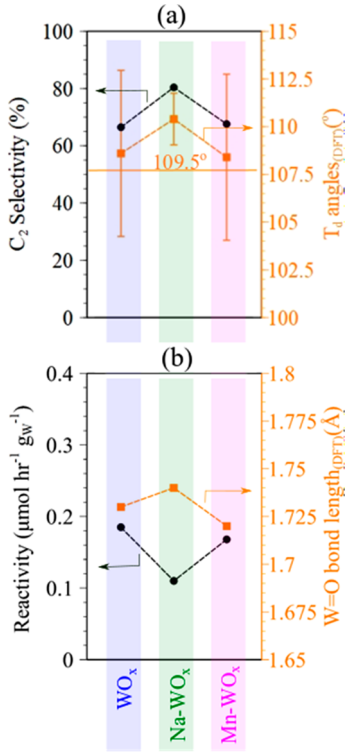

Figure 8. (a) C_2 selectivity and (b) reactivity during steady-state OCM of model catalysts. These steady-state reaction results were acquired at 830 °C, after 2 h of OCM at 1173 K with 15 mL/min of 10%O_2/90% Ar, 5 mL/min of CH_4, and 80 mL/min of Ar flow in a U-shaped quartz tube reactor. Each run utilized 30 mg of catalyst. Data are summarized in Table S4.

https://dx.doi.org/10.1021/acscatal.9b05591
ACS Catal. 2020, 10, 4580−4592

supported WO_x, Na-WO_x, and Mn-WO_x catalysts were 29.5, 34.2, and 27.3%, respectively. Interestingly, all catalysts produced more CO than CO_2, with total CO_x production being the lowest for the Na-WO_x catalyst and highest for the WO_x catalyst.

The selectivity of the catalyst was correlated to its molecular structure, as shown in Figure 8a. The addition of Na to create Na-WO_4 surface sites made the WO_x surface sites in the catalyst significantly more selective toward C_2 products. To highlight the structural promotion effect due to the Na, the DFT-calculated T_d angles (with variance shown as error bars) of the molecular structures are also plotted in Figure 8a. It can be seen that, when the surface WO_4 site exhibited a higher degree of T_d symmetry and less distortion (i.e. smaller variance), the C_2 selectivity was higher. When this is correlated with the DFT and *in situ* Raman spectroscopy data, it can be inferred that the Na-WO_x catalyst, which contains isolated Na-coordinated pseudotetrahedral WO_4 surface sites, exhibits higher selectivity toward C_2 products. As discussed, the surface Na-WO_4 sites are expected to be more symmetric than those of WO_x and Mn-WO_4 alone.

The catalyst reactivity was also correlated to its molecular structure, as shown in Figure 8b. The SiO_2-supported WO_4 catalyst exhibited the highest reactivity, followed by SiO_2-supported Mn-WO_x and Na-WO_4. Since the W═O bond is believed to participate in abstracting a proton from a CH_4 molecule,[27,47] the DFT-calculated W═O bond lengths were also plotted on the same graph. A qualitative trend can be seen where W═O bond lengths are 1.73, 1.74, and 1.72 Å for SiO_2-supported WO_4, Na-WO_4, and Mn-WO_4, respectively. The W═O bond length increase and the electron density decrease can be correlated with a decrease in reactivity of the surface sites. Notably, the Mn-WO_x/SiO_2 catalyst exhibited multiple Raman bands for the W═O vibration, signifying different environments for the WO_4 sites, which makes an exact contribution of such sites toward activating CH_4 difficult to deconvolute.

Overall, the results herein provide computational and experimental evidence that dispersed WO_4 sites exist on the SiO_2 surface and they exhibit distinct chemical properties that depend on their molecular and electronic structure. Na and Mn affect the molecular geometry of WO_4 surface sites, resulting in different reactivities and selectivities during OCM. Previously, K-coordinated WO_x/Al_2O_3 catalysts were shown to exhibit isolated surface WO_x sites with elongated W═O bonds. K was shown to prevent the formation of oligomeric surface sites with W−O−W, bridges as evidenced by the increase in UV−vis edge energy value reflecting a smaller domain size.[17,18] Provided that K^+ and Na^+ exhibit similar chemical and electronic properties, it can be proposed that Na coordination to the surface WO_4 creates isolated, pseudotetrahedral sites with higher edge energy in comparison to the uncoordinated surface WO_4 sites. Such Na-WO_4 surface sites more selectively activate CH_4 to form a CH_3* radical but do so with a penalty toward the reactivity. Importantly, such an isolated T_d site with high edge energy will most likely be absent in WO_x and Mn-WO_x catalysts, since oligomerization leads to a decrease in E_g.

Future studies on these model catalysts will be focused on *in silico*, *in situ*, and *operando* characterization of the molecular structure of the surface sites under OCM reaction conditions to relate their OCM performance to their structure. It is important to note that in the presence of Mn under O_2-lean (reducing) conditions, crystalline $MnWO_4$ forms, which contains MnO_6 and WO_6 sites even if the starting catalyst exhibited surface WO_4 sites.[46,79,80] If the same catalysts are oxidized again, however, the $MnWO_4$ structure disappears.[46,80] Consequentially, correlating the molecular site structure with OCM reactivity is only valid if the structures are present under OCM reaction conditions.

CONCLUSIONS

The DFT modeling results of isolated surface sites in uncoordinated, Na-coordinated, and Mn-coordinated tungsten oxide supported on the β-cristobalite phase of SiO_2-supported catalysts for OCM (WO_x/β-SiO_2, Na-WO_x/β-SiO_2, and Mn-WO_x/β-SiO_2) in conjunction with *ab initio* thermodynamic studies of these surface sites and experimental OCM selectivity/reactivity for the respective model catalysts were reported. In all β-SiO_2-supported catalysts modeled herein, the isolated WO_4 site (WO_4, Na-WO_4, Mn-WO_4) was found to be the most thermally stable in the OCM-relevant temperature range of 500−1300 K, with the isolated surface Na-WO_4 site being more stable than the uncoordinated WO_4 site and the Mn-coordinated WO_4 sites. Above 850 K, the Mn-WO_4 site was even less stable than the uncoordinated WO_4 site. A comparison of angles among the WO_4 units in each isolated site (WO_4, Na-WO_4, Mn-WO_4) showed that Na^+ interacted strongly with the WO_4 unit and functioned as a structural promoter, decreasing the geometric distortion in the WO_4 unit. An electronic and spin property analysis of the Mn-WO_4 system showed that the system was in the Mn^{2+}-W^{6+} electronic state, where Mn carried most of the unpaired electrons, with a small contamination of Mn^{3+}-W^{5+} also possible. The projected DOS showed that the valence band was composed of Mn 3d states, whereas the lowest part of the conduction band corresponded to W 5d states. In all cases, the DFT-calculated fundamental frequency values were in good agreement with the experimental *in situ* Raman bands under dehydrated conditions corresponding to the surface WO_4 site present in each catalyst. The steady-state OCM catalytic results in conjunction with the DFT and in situ Raman spectroscopy results show that the *dispersed phase* surface Na-WO_4 sites in the Na-WO_x catalysts exhibit lower reactivity toward CH_4 activation but significantly higher (∼15%) selectivity toward C_2 products in comparison to the WO_x and Mn-WO_x catalysts, due to the molecular geometry effects discussed in the relevant sections.

The results herein provide experimental and computational evidence for the existence of dispersed-phase isolated sites on the surface of model OCM catalysts, which previous reports have proposed on bulk crystalline phase catalysts.[40] Moreover, steady-state catalytic tests provided in this study also suggest that these isolated surface WO_4 sites exhibit tunable reactivity and selectivity toward OCM. Future work will be directed toward *in silico and in situ* characterization (Raman, XAS, UV−vis DR, XRD) of the model OCM catalysts during OCM (∼900 °C, CH_4 + O_2) to further advance the understanding of this dynamic catalytic system.

ASSOCIATED CONTENT

Supporting Information

The Supporting Information is available free of charge at https://pubs.acs.org/doi/10.1021/acscatal.9b05591.

https://dx.doi.org/10.1021/acscatal.9b05591
ACS Catal. 2020, 10, 4580−4592

Computational models used in this study, the various molecular geometries probed, and some experimental results that corroborate the data in the main text (PDF)

AUTHOR INFORMATION

Corresponding Authors

Jonas Baltrusaitis − *Department of Chemical and Biomolecular Engineering, Lehigh University, Bethlehem, Pennsylvania 18015, United States;* orcid.org/0000-0001-5634-955X; Phone: +1-610-758-6836; Email: job314@lehigh.edu

Israel E. Wachs − *Department of Chemical and Biomolecular Engineering, Lehigh University, Bethlehem, Pennsylvania 18015, United States;* orcid.org/0000-0001-5282-128X; Phone: +1-610-758-4274; Email: iew0@lehigh.edu

Authors

Daniyal Kiani − *Department of Chemical and Biomolecular Engineering, Lehigh University, Bethlehem, Pennsylvania 18015, United States;* orcid.org/0000-0002-9748-3007

Sagar Sourav − *Department of Chemical and Biomolecular Engineering, Lehigh University, Bethlehem, Pennsylvania 18015, United States;* orcid.org/0000-0001-5892-1329

William Taifan − *Department of Chemical and Biomolecular Engineering, Lehigh University, Bethlehem, Pennsylvania 18015, United States*

Monica Calatayud − *Sorbonne Université, CNRS, Laboratoire de Chimie Théorique, LCT, F-75005 Paris, France;* orcid.org/0000-0003-0555-8938

Frederik Tielens − *General Chemistry (ALGC)-Materials Modelling Group, Vrije Universiteit Brussel (Free University Brussels-VUB), 1050 Brussel, Belgium;* orcid.org/0000-0002-6760-6176

Complete contact information is available at: https://pubs.acs.org/10.1021/acscatal.9b05591

Notes

The authors declare no competing financial interest.

ACKNOWLEDGMENTS

This work was supported by NSF CBET award #1706581. The computational work herein used the Extreme Science and Engineering Discovery Environment (XSEDE),[81] which is supported by the National Science Foundation grant number ACI1053575. DK, WT and MC performed DFT calculations, D.K. and S.S. carried out experimental work, and D.K., J.B., and I.E.W. wrote the manuscript. We also acknowledge help from Dr. Mike Ford and Bin Zhang with the OCM catalytic tests.

REFERENCES

(1) Soultanidis, N.; Zhou, W.; Psarras, A. C.; Gonzalez, A. J.; Iliopoulou, E. F.; Kiely, C. J.; Wachs, I. E.; Wong, M. S. Relating n-Pentane Isomerization Activity to the Tungsten Surface Density of WOx/ZrO2. *J. Am. Chem. Soc.* **2010**, *132*, 13462−13471.

(2) Baertsch, C. D.; Komala, K. T.; Chua, Y.-H.; Iglesia, E. Genesis of Brønsted Acid Sites during Dehydration of 2-Butanol on Tungsten Oxide Catalysts. *J. Catal.* **2002**, *205*, 44−57.

(3) Santiesteban, J. G.; Vartuli, J. C.; Han, S.; Bastian, R. D.; Chang, C. D. Influence of the Preparative Method on the Activity of Highly Acidic WOx/ZrO2and the Relative Acid Activity Compared with Zeolites. *J. Catal.* **1997**, *168*, 431−441.

(4) Chen, X.; Clet, G.; Thomas, K.; Houalla, M. Correlation between structure, acidity and catalytic performance of WOx/Al2O3 catalysts. *J. Catal.* **2010**, *273*, 236−244.

(5) Olah, G. A.; Doggweiler, H.; Felberg, J. D.; Frohlich, S.; Grdina, M. J.; Karpeles, R.; Keumi, T.; Inaba, S.; Ip, W. M.; Lammertsma, K.; et al. Onium Ylide chemistry. 1. Bifunctional acid-base-catalyzed conversion of heterosubstituted methanes into ethylene and derived hydrocarbons. The onium ylide mechanism of the C1 to C2 conversion. *J. Am. Chem. Soc.* **1984**, *106*, 2143−2149.

(6) Rousseau, R.; Dixon, D. A.; Kay, B. D.; Dohnalek, Z. Dehydration, dehydrogenation, and condensation of alcohols on supported oxide catalysts based on cyclic (WO3)3 and (MoO3)3 clusters. *Chem. Soc. Rev.* **2014**, *43*, 7664−7680.

(7) Wang, H.; Wu, Y.; Liu, Z.; He, L.; Yao, Z.; Zhao, W. Deposition of WO3 on Al2O3 via a microwave hydrothermal method to prepare highly dispersed W/Al2O3 hydrodesulfurization catalyst. *Fuel* **2014**, *136*, 185−193.

(8) Schalkwyk, C. va.; Spamer, A.; Moodley, D. J.; Dube, T.; Reynhardt, J.; Botha, J. M. Application of a WO3/SiO2 catalyst in an industrial environment: part I. *Appl. Catal., A* **2003**, *255*, 121−131.

(9) Mougel, V.; Chan, K.-W.; Siddiqi, G.; Kawakita, K.; Nagae, H.; Tsurugi, H.; Mashima, K.; Safonova, O.; Copéret, C. Low Temperature Activation of Supported Metathesis Catalysts by Organosilicon Reducing Agents. *ACS Cent. Sci.* **2016**, *2*, 569−576.

(10) Engweiler, J.; Harf, J.; Baiker, A. WOx/TiO2Catalysts Prepared by Grafting of Tungsten Alkoxides: Morphological Properties and Catalytic Behavior in the Selective Reduction of NO by NH3. *J. Catal.* **1996**, *159*, 259−269.

(11) Cao, Y.; Wang, J.; Kang, M.; Zhu, Y. Catalytic conversion of glucose and cellobiose to ethylene glycol over Ni-WO3/SBA-15 catalysts. *RSC Adv.* **2015**, *5*, 90904−90912.

(12) Can, F.; Courtois, X.; Berland, S.; Seneque, M.; Royer, S.; Duprez, D. Composition dependent performance of alumina-based oxide supported WO3 catalysts for the NH3-SCR reaction and the NSR + SCR coupled process. *Catal. Today* **2015**, *257* (Part), 41−50.

(13) Lwin, S.; Li, Y.; Frenkel, A. I.; Wachs, I. E. Nature of WOx Sites on SiO2 and Their Molecular Structure−Reactivity/Selectivity Relationships for Propylene Metathesis. *ACS Catal.* **2016**, *6*, 3061−3071.

(14) Barrault, J.; Boulinguiez, M.; Forquy, C.; Maurel, R. Synthesis of methyl mercaptan from carbon oxides and H2S with tungsten—alumina catalysts. *Appl. Catal.* **1987**, *33*, 309−330.

(15) Kiani, D.; Belletti, G.; Quaino, P.; Tielens, F.; Baltrusaitis, J. Structure and Vibrational Properties of Potassium-Promoted Tungsten Oxide Catalyst Monomeric Sites Supported on Alumina (K2O/WO3/Al2O3) Characterized Using Periodic Density Functional Theory. *J. Phys. Chem. C* **2018**, *122*, 24190−24201.

(16) Grant, J. T.; Carrero, C. A.; Love, A. M.; Verel, R.; Hermans, I. Enhanced Two-Dimensional Dispersion of Group v Metal Oxides on Silica. *ACS Catal.* **2015**, *5*, 5787−5793.

(17) Kim, T.; Burrows, A.; Kiely, C. J.; Wachs, I. E. Molecular/electronic structure-surface acidity relationships of model-supported tungsten oxide catalysts. *J. Catal.* **2007**, *246*, 370−381.

(18) Zhu, M.; Li, B.; Jehng, J.-M. M.; Sharma, L.; Taborda, J.; Zhang, L.; Stach, E.; Wachs, I. E.; Wu, Z.; Baltrusaitis, J. Molecular structure and sour gas surface chemistry of supported K2O/WO3/Al2O3catalysts. *Appl. Catal., B* **2018**, *232*, 146−154.

(19) Lee, E. L.; Wachs, I. E. Situ Spectroscopic Investigation of the Molecular and Electronic Structures of SiO2 Supported Surface Metal Oxides. *J. Phys. Chem. C* **2007**, *111*, 14410−14425.

(20) Ross-Medgaarden, E. I.; Knowles, W. V.; Kim, T.; Wong, M. S.; Zhou, W.; Kiely, C. J.; Wachs, I. E. New insights into the nature of the acidic catalytic active sites present in ZrO2-supported tungsten oxide catalysts. *J. Catal.* **2008**, *256*, 108−125.

(21) Ross-medgaarden, E. I.; Wachs, I. E. Structural determination of bulk and surface tungsten oxides with UV-vis diffuse reflectance spectroscopy and raman spectroscopy. *J. Phys. Chem. C* **2007**, *111*, 15089−15099.

(22) Wachs, I. E. Recent conceptual advances in the catalysis science of mixed metal oxide catalytic materials. *Catal. Today* **2005**, *100*, 79−94.
(23) Lwin, S.; Wachs, I. E. Catalyst Activation and Kinetics for Propylene Metathesis by Supported WOx/SiO2Catalysts. *ACS Catal.* **2017**, *7*, 573−580.
(24) Lwin, S.; Li, Y.; Frenkel, A. I.; Wachs, I. E. Nature of WOxSites on SiO2and Their Molecular Structure-Reactivity/Selectivity Relationships for Propylene Metathesis. *ACS Catal.* **2016**, *6*, 3061−3071.
(25) Yeh, Y.-H.; Rzepa, C.; Rangarajan, S.; Gorte, R. J. Influence of brønsted-acid and cation-exchange sites on ethene adsorption in ZSM-5. *Microporous Mesoporous Mater.* **2019**, *284*, 336−342.
(26) Taifan, W.; Baltrusaitis, J. CH4 conversion to value added products: Potential, limitations and extensions of a single step heterogeneous catalysis. *Appl. Catal., B* **2016**, *198*, 525−547.
(27) Schwach, P.; Pan, X.; Bao, X. Direct Conversion of Methane to Value-Added Chemicals over Heterogeneous Catalysts: Challenges and Prospects. *Chem. Rev.* **2017**, *117*, 8497−8520.
(28) Arndt, S.; Otremba, T.; Simon, U.; Yildiz, M.; Schubert, H.; Schomäcker, R. Mn−Na2WO4/SiO2 as catalyst for the oxidative coupling of methane. What is really known? *Appl. Catal., A* **2012**, *425*−*426*, 53−61.
(29) Wang, B.; Albarracín-Suazo, S.; Pagán-Torres, Y.; Nikolla, E. Advances in methane conversion processes. *Catal. Today* **2017**, *285*, 147−158.
(30) Pak, S.; Lunsford, J. H. Thermal effects during the oxidative coupling of methane over Mn/Na 2 WO 4/SiO 2 and Mn/Na 2 WO 4/MgO catalysts. *Appl. Catal., A* **1998**, *168*, 131−137.
(31) Karakaya, C.; Kee, R. J. Progress in the direct catalytic conversion of methane to fuels and chemicals. *Prog. Energy Combust. Sci.* **2016**, *55*, 60−97.
(32) Palermo, A.; Holgado Vazquez, J. P.; Lee, A. F.; Tikhov, M. S.; Lambert, R. M. Critical influence of the amorphous silica-to-cristobalite phase transition on the performance of Mn/Na2WO4/SiO2 catalysts for the oxidative coupling of methane. *J. Catal.* **1998**, *177*, 259−266.
(33) Wang, D. J.; Rosynek, M. P.; Lunsford, J. H. Oxidative Coupling of Methane over Oxide-Supported Sodium-Manganese Catalysts. *J. Catal.* **1995**, *155*, 390−402.
(34) Farrell, B. L.; Igenegbai, V. O.; Linic, S. A Viewpoint on Direct Methane Conversion to Ethane and Ethylene Using Oxidative Coupling on Solid Catalysts. *ACS Catal.* **2016**, *6*, 4340−4346.
(35) Zavyalova, U.; Holena, M.; Schlögl, R.; Baerns, M. Statistical analysis of past catalytic data on oxidative methane coupling for new insights into the composition of high-performance catalysts. *ChemCatChem* **2011**, *3*, 1935−1947.
(36) Jiang, Z. C.; Yu, C. J.; Fang, X. P.; Li, S. B.; Wang, H. L. Oxide/support interaction and surface reconstruction in the sodium tungstate(Na2WO4)/silica system. *J. Phys. Chem.* **1993**, *97*, 12870−12875.
(37) Wu, J.; Li, S. The Role of Distorted W04 in the Oxidative Coupling of Methane on Tungsten Oxide Supported Catalysts. *J. Phys. Chem.* **1995**, *99*, 4566−4568.
(38) Ji, S.; Xiao, T.; Li, S.; Chou, L.; Zhang, B.; Xu, C.; Hou, R.; York, A. P. E. E.; Green, M. L. H. H. Surface WO4 tetrahedron: The essence of the oxidative coupling of methane over M-W-Mn/SiO2catalysts. *J. Catal.* **2003**, *220*, 47−56.
(39) Palermo, A.; Pedro, J.; Vazquez, H.; Lambert, R. M. New efficient catalysts for the oxidative coupling of methane. *Catal. Lett.* **2000**, *68*, 191−196.
(40) Kiani, D.; Sourav, S.; Baltrusaitis, J.; Wachs, I. E. Oxidative Coupling of Methane (OCM) by SiO2-Supported Tungsten Oxide Catalysts Promoted with Mn and Na. *ACS Catal.* **2019**, *9*, 5912−5928.
(41) Wachs, I. E.; Jehng, J.-M.; Ueda, W. Determination of the Chemical Nature of Active Surface Sites Present on Bulk Mixed Metal Oxide Catalysts. *J. Phys. Chem. B* **2005**, *109*, 2275−2284.
(42) Phivilay, S. P.; Roberts, C. A.; Puretzky, A. A.; Domen, K.; Wachs, I. E. Fundamental Bulk/Surface Structure − Photoactivity Relationships of Supported $\{Rh_{(2-y)}Cr_{(y)}O_3\}$/GaN Photocatalysts. *J. Phys. Chem. Lett.* **2013**, *4*, 3719−3724.
(43) Phivilay, S. P.; Puretzky, A. A.; Domen, K.; Wachs, I. E. Nature of Catalytic Active Sites Present on the Surface of Advanced Bulk Tantalum Mixed Oxide Photocatalysts. *ACS Catal.* **2013**, *3*, 2920−2929.
(44) Zhu, M.; Tian, P.; Kurtz, R.; Lunkenbein, T.; Xu, J.; Schlögl, R.; Wachs, I. E.; Han, Y.-F. Strong Metal−Support Interactions between Copper and Iron Oxide during the High-Temperature Water-Gas Shift Reaction. *Angew. Chem., Int. Ed.* **2019**, *58*, 9083−9087.
(45) Vamvakeros, A.; Jacques, S. D. M.; Middelkoop, V.; Di Michiel, M.; Egan, C. K.; Ismagilov, I. Z.; Vaughan, G. B. M.; Gallucci, F.; van Sint Annaland, M.; Shearing, P. R.; et al. Real time chemical imaging of a working catalytic membrane reactor during oxidative coupling of methane. *Chem. Commun.* **2015**, *51*, 12752−12755.
(46) Pengwei, W.; Guofeng, Z.; Wang, Y.; Yong, L.; Wang, P.; Zhao, G.; Wang, Y.; Lu, Y. MnTiO3-driven low-temperature oxidative coupling of methane over TiO2-doped Mn2O3-Na2WO4/SiO2catalyst. *Sci. Adv.* **2017**, *3*, e1603180.
(47) Kiani, D.; Sourav, S.; Baltrusaitis, J.; Wachs, I. E. The Oxidative Coupling of Methane (OCM) by SiO2-Supported Tungsten Oxide Catalysts Promoted with Mn and Na. *ACS Catal.* **2019**, *9*, 5912−5928.
(48) Howell, J. G.; Li, Y.; Bell, A. T. Propene Metathesis over Supported Tungsten Oxide Catalysts: A Study of Active Site Formation. *ACS Catal.* **2016**, *6*, 7728−7738.
(49) Kim, D. S.; Ostromecki, M.; Wachs, I. E.; Kohler, S. D.; Ekerdt, J. G. Preparation and characterization ofWO3/SiO2 catalysts. *Catal. Lett.* **1995**, *33*, 209−215.
(50) Byrnes, A. P.; Wyllie, P. J. Subsolidus and melting relations for the join CaCO3-MgCO3 at 10 kbar. *Geochim. Cosmochim. Acta* **1981**, *45*, 321−328.
(51) Spearing, D. R.; Farnan, I.; Stebbins, J. F. Dynamics of the Alpha-Beta Phase-Transitions in Quartz and Cristobalite as Observed by Insitu High-Temperature Si-29 Nmr and O-17 Nmr. *Phys. Chem. Miner.* **1992**, *19*, 307−321.
(52) Damby, D. E.; Llewellin, E. W.; Horwell, C. J.; Williamson, B. J.; Najorka, J.; Cressey, G.; Carpenter, M. The a − b phase transition in volcanic cristobalite research papers. *J. Appl. Crystallogr.* **2014**, *47*, 1205−1215.
(53) Hatch, D. M.; Ghose, S. The A-β Phase Transition in Cristobalite, SiO2.pdf. *Phys. Chem. Miner.* **1991**, *17*, 554−562.
(54) Meike, A.; Glassley, W. E. In-Situ Observation of the Alpha/beta Cristobalite Transition Using High Voltage Electron Microscopy. *MRS Proc.* **1989**, *176*, 631.
(55) Downs, R. T.; Palmer, D. C. The pressure behavior of a cristobalite. *Am. Mineral.* **1994**, *79*, 9−14.
(56) Wright, A. F.; Leadbetter, A. J. The structures of the β-cristobalite phases of SiO2 and AlPO4. *Philos. Mag.* **1975**, *31*, 1391−1401.
(57) Shubin, A.; Zilberberg, I.; Ismagilov, I.; Matus, E.; Kerzhentsev, M.; Ismagilov, Z. Hydrogen abstraction from methane on cristobalite supported W and Mn oxo complexes: A DFT study. *Mol. Catal.* **2018**, *445*, 307−315.
(58) Chen, H.-S.; Niu, J.-Z.; Zhang, B.; Li, S.-B. DFT Study on the Active Sites in Mn-Na2WO4/SiO2 Catalyst. *Acta Phys.-Chim. Sin.* **2001**, *17*, 111−115.
(59) Kresse, G.; Joubert, D. From ultrasoft pseudopotentials to the projector augmented-wave method. *Phys. Rev. B: Condens. Matter Mater. Phys.* **1999**, *59*, 1758−1775.
(60) Kresse, G.; Furthmüller, J. Efficient iterative schemes for *ab initio* total-energy calculations using a plane-wave basis set. *Phys. Rev. B: Condens. Matter Mater. Phys.* **1996**, *54*, 11169−11186.
(61) Kresse, G.; Hafner, J. Ab initio molecular dynamcis for liquid metals. *Phys. Rev. B: Condens. Matter Mater. Phys.* **1993**, *47* (1), 558.
(62) Kresse, G.; Furthmiiller, J. Efficiency of ab-initio total energy calculations for metals and semiconductors using a plane-wave basis set. *Comput. Mater. Sci.* **1996**, *6*, 15−50.

https://dx.doi.org/10.1021/acscatal.9b05591
ACS Catal. 2020, 10, 4580−4592

(63) Perdew, J. P.; Chevary, J. A.; Vosko, S. H.; Jackson, K. A.; Pederson, M. R.; Singh, D. J.; Fiolhais, C.; Chevary, J. A.; Vosko, S. H.; Jackson, K. A.; et al. Atoms, molecules, solids, and surfaces: Applications of the generalized gradient approximation for exchange and correlation. *Phys. Rev. B: Condens. Matter Mater. Phys.* **1992**, *46*, 6671−6687.
(64) Guesmi, H.; Grybos, R.; Handzlik, J.; Tielens, F. Characterization of tungsten monomeric oxide species supported on hydroxylated silica; A DFT study. *RSC Adv.* **2016**, *6*, 39424−39432.
(65) Frisch, M. J.; Trucks, G. W.; Schlegel, H. B.; Scuseria, G. E.; Robb, M. A.; Cheeseman, J. R.; Montgomery, J. A., Jr.; Vreven, T.; Kudin, K. N.; Burant, J. C.; Millam, J. M.; Iyengar, S. S.; Tomasi, J.; Barone, V.; Mennucci, B.; Cossi, M.; Scalmani, G., et al.*Gaussian 03*; Gaussian Inc.: Wallingford, CT,2004.
(66) *CRC Handbook of Chemistry and Physics*, 85th ed.; Lide, D. R., Ed.; CRC Press: 2004, pp 6−8.
(67) Handzlik, J.; Ogonowski, J. Structure of isolated molybdenum-(VI) and molybdenum(IV) oxide species on silica: Periodic and cluster DFT studies. *J. Phys. Chem. C* **2012**, *116*, 5571−5584.
(68) Kim, D. S.; Ostromecki, M.; Wachs, I. E. Surface structures of supported tungsten oxide catalysts under dehydrated conditions. *J. Mol. Catal. A: Chem.* **1996**, *106*, 93−102.
(69) Wachs, I. E.; Kim, T.; Ross, E. I. Catalysis science of the solid acidity of model supported tungsten oxide catalysts. *Catal. Today* **2006**, *116*, 162−168.
(70) Andriopoulou, C.; Boghosian, S. Tuning the configuration of dispersed oxometallic sites in supported transition metal oxide catalysts: A temperature dependent Raman study. *Catal. Today* **2019**, *336*, 74−83.
(71) Ji, S.-f.; Xiao, T.-c.; Li, S.-b.; Xu, C.-z.; Hou, R.-l.; Coleman, K. S; Green, M. L. H. The relationship between the structure and the performance of Na-W-Mn/SiO2 catalysts for the oxidative coupling of methane. *Appl. Catal., A* **2002**, *225*, 271−284.
(72) Hardcastle, F. D.; Wachs, I. E. Determination of the Molecular Structures of Tungstates by Raman Spectroscopy. *J. Raman Spectrosc.* **1995**, *26*, 397−405.
(73) Riedel, W.; Thum, L.; Möser, J.; Fleischer, V.; Simon, U.; Siemensmeyer, K.; Schnegg, A.; Schomäcker, R.; Risse, T.; Dinse, K.-P. Magnetic Properties of Reduced and Reoxidized Mn−Na_2WO_4/SiO_2: A Catalyst for Oxidative Coupling of Methane (OCM). *J. Phys. Chem. C* **2018**, *122*, 22605−22614.
(74) Henkelman, G.; Arnaldsson, A.; Jónsson, H. A fast and robust algorithm for Bader decomposition of charge density. *Comput. Mater. Sci.* **2006**, *36*, 354−360.
(75) Koca, J.; Jirouskova, Z.; Svobodova Varekova, R.; Vanek, J. Electronegativity Equalization Method: Parameterization and Validation for Organic Molecules Using the Merz-Kollman-Singh Charge Distribution Scheme. *J. Comput. Chem.* **2009**, *30*, 1174−1178.
(76) Yu, M.; Trinkle, D. R. Accurate and efficient algorithm for Bader charge integration. *J. Chem. Phys.* **2011**, *134*, No. 064111.
(77) Hoang, K. Polaron formation, native defects, and electronic conduction in metal tungstates. *Phys. Rev. Mater.* **2017**, *1*, 2−9.
(78) Fortes, A. D. Crystal structures of spinel-type Na2MoO4 and Na2WO4 revisited using neutron powder diffraction. *Acta Crystallogr. Sect. E Crystallogr. Commun.* **2015**, *71*, 592−596.
(79) Hayek, N. S.; Khlief, G. J.; Horani, F.; Gazit, O. M. Effect of reaction conditions on the oxidative coupling of methane over doped MnOx-Na2WO4/SiO2 catalyst. *J. Catal.* **2019**, *376*, 25−31.
(80) Wang, P.; Zhao, G.; Liu, Y.; Lu, Y. TiO2-doped Mn2O3-Na2WO4/SiO2 catalyst for oxidative coupling of methane: Solution combustion synthesis and MnTiO3-dependent low-temperature activity improvement. *Appl. Catal., A* **2017**, *544*, 77−83.
(81) Towns, J.; Cockerill, T.; Dahan, M.; Foster, I.; Gaither, K.; Grimshaw, A.; Hazlewood, V.; Lathrop, S.; Lifka, D.; Peterson, G. D. XSEDE: Accelerating Scientific Discovery. *Comput. Sci. Eng.* **2014**, *16*, 62.

https://dx.doi.org/10.1021/acscatal.9b05591
ACS Catal. 2020, 10, 4580−4592